Available online at www.sciencedirect.com
ScienceDirect
Nuclear Instruments and Methods in Physics Research A 574 (2007) 98–109
NUCLEAR INSTRUMENTS & METHODS IN PHYSICS RESEARCH Section A
www.elsevier.com/locate/nima

Gamma-ray energy-imaging integrated spectral deconvolution ☆

D. Xu*, Z. He[1]

Department of Nuclear Engineering and Radiological Sciences, University of Michigan, Ann Arbor, Michigan, USA

Received 6 September 2006; received in revised form 29 December 2006; accepted 25 January 2007
Available online 11 February 2007

Abstract

In conventional Compton camera systems, the image reconstruction is performed only in two-dimensional or three-dimensional spatial coordinates for a specific gamma-ray energy. By doing so, a priori knowledge of the incident gamma-ray energy is required, and usually an energy window is applied to select full energy deposition events. In some other applications, spectral-deconvolution algorithms were developed to estimate the incident gamma-ray spectrum by deconvolving the observed energy-loss spectrum. However, usually the spectral system response function of a non-spherical detector depends on the incident gamma-ray's direction, which cannot be modeled by those spectral-deconvolution algorithms. In this paper, we propose a new energy-imaging integrated spectral-deconvolution method, which utilizes both the Compton imaging and the spectral-deconvolution techniques. In the new method, the deconvolution takes place in a integrated spatial and energy space. This technique eliminates the requirement of knowing the gamma-ray energy in the imaging part, and removes the directional dependence in the spectral-deconvolution part. The deconvolved result provides the image at any specific energy, as well as the spectrum at any specific direction. The deconvolution method is based on the maximum likelihood expectation maximization (MLEM) algorithm, which is popular in reconstructing photon-emission images. Since the ML solution estimates the true incident gamma-ray intensity, the deconvolved energy spectrum at the source location is free of Compton continuum. To truthfully reconstruct the source distribution from the observation data, the accuracy of the system response function t_{ij}, i.e. the probability for a photon from source pixel **j** to be observed as event **i**, is the most crucial information. Because of the large number of pixels in the energy-imaging integrated space, and the very large number of possible measurement events, it is impossible to pre-calculate the system response function t_{ij} by simulations. In this paper, an analytical approach is introduced so that the system response function can be calculated during the reconstruction process. In order to perform Compton imaging, gamma-ray detectors are required to have position-sensing capability. The energy-imaging integrated deconvolution algorithm is applied to a three-dimensional position-sensitive CdZnTe gamma-ray imaging spectrometer, which can provide not only the energy-deposition information, but also the position information of individual gamma-ray interactions. The results demonstrate that the technique is capable of deconvolving the energy spectrum and of reconstructing the image simultaneously.

Keywords: Compton imaging; Spectral deconvolution; MLEM; System response function

1. Introduction

A gamma-ray Compton camera captures two or more interactions of an incident photon and records the position and energy information of each interaction. The scattering angle θ can be obtained from the deposited energies by the Compton scattering formula of

$$\cos\theta = 1 - \frac{m_e c^2 E_1}{E_0(E_0 - E_1)} \quad (1)$$

where $m_e c^2$ is the rest mass energy of an electron, E_0 is the initial gamma-ray energy, and E_1 is the energy deposited in the Compton scattering. The direction of the scattered photon can be obtained from the interaction positions. Therefore, the direction of each incident photon is constrained on the surface of a cone with its vertex placed at the first interaction location, and the axis of the cone is

☆This work was supported in part by the U.S. Department of Energy/NNSA NA-22 Office under Grant No. DE-FG52-01-NN20122.
*Corresponding author.
E-mail addresses: xud@umich.edu, xud@ge.com (D. Xu), hezhong@umich.edu (Z. He).
[1]Present address: 2355 Bonisteel Boulevard, Ann Arbor, MI 48109-2104, USA.

0168-9002/$ - see front matter © 2007 Elsevier B.V. All rights reserved.
doi:10.1016/j.nima.2007.01.171

determined by the first and the second interaction positions, as shown in Fig. 1. Since the back-projection cone of each event passes the true source location, the source image can be reconstructed when many cones overlap with each other.

In conventional Compton imaging systems, it is sometimes assumed that the incident gamma-ray energy is known a priori. To reduce the Compton background, an image is typically reconstructed only from those events within a narrow energy window. However, in many applications, the energy of the incident gamma-ray is unknown, or the energy spectrum is continuous, and it is unlikely to set an energy window to select the full energy events. Therefore, the reconstructed image is degraded by the Compton background, in which only a fraction of the incident photon's energy is deposited within the detector. Even if the incident gamma-ray energy is known, in the case of multiple sources, the low-energy photopeak is contaminated by the Compton background from the high-energy sources, and the reconstructed image of the low-energy gamma-rays is affected by the distribution of the high-energy gamma-rays. Furthermore, although the back-projection rings of the Compton background do not pass the true source direction, those background events still contain information about the source distribution. Therefore, there will be a waste in efficiency if only full energy events are reconstructed.

In order to obtain the true incident gamma-ray spectra given the measured energy loss spectra and the detector system response function, spectral deconvolution methods were developed for gamma-ray spectroscopy [1,2]. Those deconvolution methods are performed only on energy spectra. Since the responses of most actual gamma-ray detectors depend on the incident direction of gamma-rays, those methods are fundamentally vulnerable to spatially distributed sources.

As the advances in modern gamma-ray detector developments, more and more detector systems begin to have position-sensing capabilities. The interaction of position information can provide extra information about the direction of the incident gamma-rays by means of Compton imaging. Therefore, the detector system response function can be modeled as a function of the incident gamma-ray's direction for those measured events with multiple interactions. In this paper, we describe a new energy-imaging integrated deconvolution algorithm in which the techniques of Compton imaging and spectral deconvolution are integrated together. The deconvolution space is defined as a combined space of both energy and spatial dimensions. By this means, this method can simultaneously provide the source image at any gamma-ray energy, as well as the gamma-ray energy spectrum at any incident direction. By applying the new deconvolution algorithm, the Compton continuum in the spectrum will contribute to the full energy peak, and a priori knowledge of the incident gamma-ray's energy is no longer required. Since the directional dependence can be modeled by the system response function, the new algorithm can be applied to spatially distributed sources.

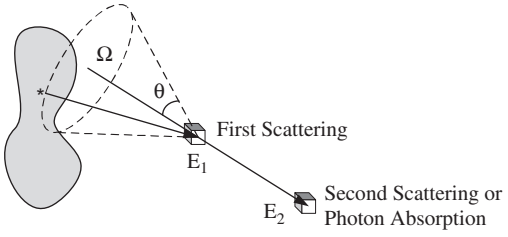

Fig. 1. If a gamma-ray interacts at least twice in the detector, the direction of the incident gamma-ray can be constrained on the surface of a cone. The half angle is determined by the energy losses, the cone vertex is placed at the first interaction position, and the cone axis is defined by the first and the second interaction positions.

Among various spectral-deconvolution algorithms, the maximum likelihood expectation maximization (MLEM) algorithm was proven to be superior [2]. In the proposed energy-imaging integrated deconvolution algorithm, a pixel **j** is defined in a combined space of both spatial and energy dimension, and a measurement **i** is defined by two sets of position and energy information. Suppose the position is defined on an $11 \times 11 \times 10$ grid, and the energy is divided into 1000 channels, as a result, there will be more than 10^6 bins in each set of position and energy information. A Compton scattered event requires at least two sets of position and energy information. As a result, 10^{12} bins are required to store the measurement output, which is beyond the limit of any memory system currently available. To overcome the difficulty, list-mode MLEM is implemented instead of general MLEM algorithm. The list-mode MLEM algorithm is performed using the iterative equation of [3–5]:

$$\lambda_j^{n+1} = \frac{\lambda_j^n}{s_j} \sum_{i=1}^{N} \frac{t_{ij}}{\sum_k t_{ik} \lambda_k^n} \tag{2}$$

in which λ_j^n is the estimated value of pixel **j** at nth iteration, the sensitivity image s_j is the probability of a gamma-ray emission from pixel **j** to be detected, N is the total number of measured events, and the system response function t_{ij} is the probability of a gamma-ray emission from pixel **j** to be observed as measurement **i**.

Because of the huge number of possible measurement events, it is impossible to pre-calculate the system response function t_{ij} by simulations. In this paper, Section 2 describes an analytical model to calculate the system response function for each measured event during the reconstruction process. This analytical approach considers the binning process and the uncertainties in an actual detector system. Since the imaging space includes the energy dimension, there are two possibilities for a photon from an imaging pixel to create a measured event with two interactions. The first possibility is that the photon deposits all its energy in the detector by a Compton scattering followed by a photoelectric absorption. The other possibility is that the photon deposits part of its energy by two

Compton scatterings and the scattered photon escapes. The system response function model should account for both possibilities. This way, the measured Compton background will contribute to the photopeak. With an accurate system response function, the deconvolved energy spectrum will be the estimation of the true intensity of the incident gamma-rays, thus free of Compton scattering continuum.

The sensitivity image s_j can be obtained by summing the rows of the system response function t_{ij}, i.e.

$$s_j = \sum_i t_{ij}. \tag{3}$$

However, because of the huge number of possible measurement outputs, the direct approach of Eq. (3) is not practical. In this work, the sensitivity image s_j is obtained by simulations.

Three-dimensional position-sensitive CdZnTe detector is a novel room-temperature semiconductor gamma-ray spectrometer. It was initially developed to achieve good energy resolution even if the detector material is not uniform and has charge trapping problems. This is because the true energy deposition can be obtained by correcting the measured pulse amplitude as a function of the three-dimensional position of interactions [6,7]. However, the capability of position sensing, as well as the excellent energy resolution, enables three-dimensional CdZnTe detector systems to perform Compton imaging [8,9]. The size of the detector is $15 \times 15 \times 10\,\text{mm}^3$. The anode of the CdZnTe detector is divided into an 11×11 pixel array Fig. 2. The lateral coordinates are given by the location of individual anode pixels collecting electrons, and the interaction depth is measured by the drift time of electrons from the interaction position to the collecting anode. The depth resolution is about 0.5 mm, which makes the position resolution of the CdZnTe detector about $1\,\text{mm}^3$. If a gamma-ray interacts multiple times in the detector, the individual interactions will be registered by different pixels. Therefore, each measured event may have different numbers of pixels which have energy depositions. The measured events are grouped into single-pixel events, two-pixel events, three-pixel events, etc. With the capability of registering multiple interactions, a single detector is capable of performing Compton imaging. A $15 \times 15 \times 10\,\text{mm}^3$ CdZnTe detector was applied to demonstrate that the energy-imaging integrated algorithm is capable of deconvolving the energy spectrum and of reconstructing the image simultaneously. Since there is no mechanical collimator required, the spatial imaging space is the 4π angular space around the detector.

2. Energy-imaging integrated system response function

The system response function t_{ij} is defined as the probability of a photon emitted from pixel **j** to be observed as a measured event **i**. Here, a pixel **j** is defined in the combined spatial and energy space. The system response function t_{ij} therefore can be described as the probability of a photon with a certain energy emitted from a certain spatial direction to be observed as event **i**.

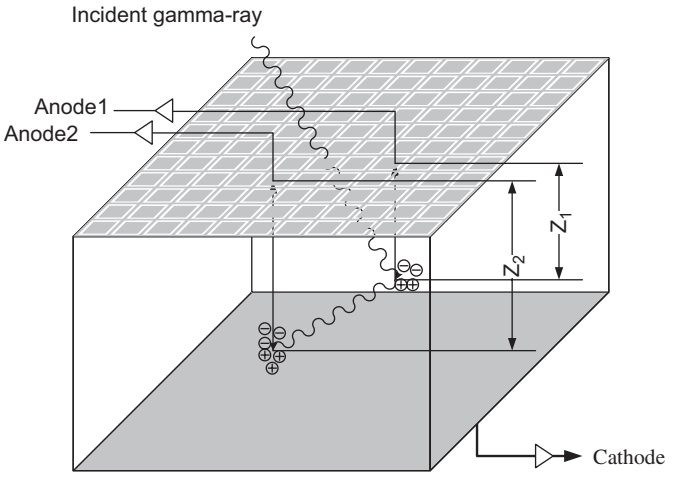

Fig. 2. Three-dimensional position-sensitive CdZnTe detector. The size of the detector is $15 \times 15 \times 10\,\text{mm}^3$.

The measurement data are usually binned due to pixellation or digitization. Therefore, the measurement result is actually a small bin volume around point **i** in the measurement space, which is defined by a set of position and energy attributes given by the detector system. Before this binning process, the imperfect detector system will introduce uncertainties to the measurement quantities due to noise or Doppler broadening. Therefore, the system response function can be written as

$$t_{ij} = \int_{\Delta \mathbf{V}_\mathbf{i}} \mathrm{d}\hat{\mathbf{i}} \int f(\hat{\mathbf{i}}|\tilde{\mathbf{i}}) f(\tilde{\mathbf{i}}|\mathbf{j})\,\mathrm{d}\tilde{\mathbf{i}} \tag{4}$$

in which, $f(\tilde{\mathbf{i}}|\mathbf{j})$ is the probability density function for a photon from pixel **j** to create a 'real' event $\tilde{\mathbf{i}}$, which consists of the actual interaction positions and deposited energies, and $f(\hat{\mathbf{i}}|\tilde{\mathbf{i}})$ is the probability for the detector system to generate a response of $\hat{\mathbf{i}}$ due to uncertainties given the real event $\tilde{\mathbf{i}}$. $\Delta \mathbf{V}_i$ is the bin volume around measurement **i**.

Our model is based on the following procedure to calculate the system response function. First, we derive the probability density function $f(\tilde{\mathbf{i}}|\mathbf{j})$ for a photon emitted from pixel **j** to create a real event $\tilde{\mathbf{i}}$. Then we calculate the probability density function $f(\hat{\mathbf{i}}|\tilde{\mathbf{i}})$ for the detector system to output this real event $\tilde{\mathbf{i}}$ as a measured event $\hat{\mathbf{i}}$ in the measurement space due to uncertainties, assuming all the uncertainties are Gaussian. Finally, to obtain t_{ij}, the probability density function is integrated over the bin volume $\Delta \mathbf{V}_i$ around **i**.

In this work, only two-interaction events are modeled. The system response function modeling for three or more interaction events can follow the same procedures but usually is much more complicated. The spatial domain in the imaging space is the 4π angular space around the detector, thus a source pixel in the energy-imaging integrated space is defined by $(E_0, \mathbf{\Omega}_0)$. The deconvolved image gives the incident gamma-ray intensity from a

certain direction, which is irrelevant to the distance between the source and the detector. Therefore, it is reasonable to assume that the source is distributed on the surface of a sphere with radius R which is much greater than the dimension of the detector. As a result, a source pixel can also be described by $(E_0, \mathbf{r}_0)$, in which $\mathbf{r}_0 = R\mathbf{\Omega}_0$. The measurement event $\tilde{\mathbf{i}}$ and $\hat{\mathbf{i}}$ can be represented by $(\tilde{E}_1, \tilde{\mathbf{r}}_1, \tilde{E}_2, \tilde{\mathbf{r}}_2)$ and $(\hat{E}_1, \hat{\mathbf{r}}_1, \hat{E}_2, \hat{\mathbf{r}}_2)$, respectively. Fig. 3 illustrates a two-interaction event. d_1 is the distance that the incident photon travels before reaching the first interaction position, d is the distance between the two-interaction positions, and d_2 is the distance that the escaping photon travels before leaving the detector.

2.1. Probability density function of $f(\tilde{\mathbf{i}}|\mathbf{j})$

In a measured event, if two interactions are observed by the detector system, the first interaction is assumed to be a Compton scattering. For the second interaction, there are two possibilities, which are another Compton scattering or a photoelectric absorption. The general case is discussed below.

The directions of the incident and scattered photons are defined by $\tilde{\mathbf{\Omega}}_1 = (\tilde{\mathbf{r}}_1 - \mathbf{r}_0)/|\tilde{\mathbf{r}}_1 - \mathbf{r}_0|$, and $\tilde{\mathbf{\Omega}}_2 = (\tilde{\mathbf{r}}_2 - \tilde{\mathbf{r}}_1)/|\tilde{\mathbf{r}}_2 - \tilde{\mathbf{r}}_1|$. We have the following conditional probability:

$$f(\tilde{\mathbf{\Omega}}_2|E_0, \tilde{E}_1, \tilde{\mathbf{\Omega}}_1) = \frac{\delta(\theta_r - \theta_e)}{2\pi \sin\theta_e} \tag{5}$$

in which θ_e is the scattering angle determined by energies E_0 and E_1 (Eq. (1)), θ_r is the angle between $\tilde{\mathbf{\Omega}}_1$ and $\tilde{\mathbf{\Omega}}_2$, and $\delta(\theta_r - \theta_e)$ is the Dirac delta function. Eq. (5) means that given the direction and the initial energy of the incident photon, and the energy deposited in the first scattering, the second interaction must occur on the surface of a cone with half angle determined by Compton scattering kinematics (here, coherent scattering, Doppler broadening and polarization are neglected).

We introduce t as the distance that the scattered photon travels before the second interaction. If t is known, the second scattering must occur on a ring which is on the cone defined by Eq. (5). Since $\tilde{\mathbf{\Omega}}_1$ and $\tilde{\mathbf{\Omega}}_2$ are defined by $\tilde{\mathbf{r}}_0$, $\tilde{\mathbf{r}}_1$ and $\tilde{\mathbf{r}}_2$, from Eq. (5) we have

$$f(\tilde{\mathbf{r}}_2|E_0, \mathbf{r}_0, \tilde{E}_1, \tilde{\mathbf{r}}_1, t) = \frac{\delta(\theta_r - \theta_e)\delta(d - t)}{2\pi t^2 \sin\theta_e}. \tag{6}$$

The probability density function for a photon with energy E_0 from $\mathbf{r}_0$ to interact at position $\tilde{\mathbf{r}}_1$ is

$$f(\tilde{\mathbf{r}}_1|E_0, \mathbf{r}_0) = \frac{1}{4\pi R^2}\, \mu_{E_0} e^{-\mu_{E_0} d_1} \tag{7}$$

in which $1/4\pi R^2$ is the solid angle and μ_E is the linear attenuation coefficient for gamma-rays at energy E.

The probability density function for a photon from $(E_0,\ \mathbf{r}_0)$ to deposit $\tilde{E}_1$ in a Compton scattering given the condition that the photon interacts at position $\tilde{\mathbf{r}}_1$ is

$$\begin{aligned} f(\tilde{E}_1|E_0, \mathbf{r}_0, \tilde{\mathbf{r}}_1) &= \frac{1}{\sigma_t(E_0)} \frac{d\sigma_c(E_0)}{d\Omega}\bigg|_{\tilde{E}_1} \frac{d\Omega}{d\tilde{E}_1}\bigg|_{\tilde{E}_1} \\ &= \frac{N}{\mu_{E_0}} \frac{d\sigma_c(E_0)}{d\Omega}\bigg|_{\tilde{E}_1} \frac{d\Omega}{d\tilde{E}_1}\bigg|_{\tilde{E}_1} \end{aligned} \tag{8}$$

in which, $\sigma_t(E)$ is the total cross-section at energy E, N is the number of nuclei per unit volume, and $d\sigma_c(E_0)/d\Omega$ is the differential scattering cross-section defined by the Klein–Nishina formula.

The probability density function for the scattered photon to travel a distance of t before the second interaction is

$$f(t|E_0, \mathbf{r}_0, \tilde{E}_1, \tilde{\mathbf{r}}_1) = \mu_{E_0 - E_1}\, e^{-\mu_{E_0 - E_1} t}. \tag{9}$$

From Eqs. (7), (8), and (9), we can obtain

$$\begin{aligned} &f(\tilde{E}_1, \tilde{\mathbf{r}}_1, t|E_0, \mathbf{r}_0) \\ &\quad = f(t|E_0, \mathbf{r}_0, \tilde{E}_1, \tilde{\mathbf{r}}_1) f(\tilde{E}_1|E_0, \mathbf{r}_0, \tilde{\mathbf{r}}_1) f(\tilde{\mathbf{r}}_1|E_0, \mathbf{r}_0) \\ &\quad = \frac{1}{4\pi R^2}\, e^{-\mu_{E_0} d_1} N \frac{d\sigma_c(E_0)}{d\Omega}\bigg|_{\tilde{E}_1} \frac{d\Omega}{d\tilde{E}_1}\bigg|_{\tilde{E}_1} \mu_{E_0 - \tilde{E}_1} e^{-\mu_{E_0 - \tilde{E}_1} t} \end{aligned} \tag{10}$$

which is the probability density function that a photon with energy E_0 and from $\mathbf{r}_0$ creates the first scattering interaction of $(\tilde{E}_1, \tilde{\mathbf{r}}_1)$ and the scattered photon travels a distance of t before the second interaction.

From Compton scattering kinematics, we have

$$d\Omega = 2\pi \sin\theta\, d\theta = \frac{2\pi m_e c^2}{(E_0 - E_1)^2}\, dE_1. \tag{11}$$

From Eqs. (6), (10), and (11), we obtain

$$\begin{aligned} &f(\tilde{E}_1, \tilde{\mathbf{r}}_1, t, \tilde{\mathbf{r}}_2|E_0, \mathbf{r}_0) \\ &\quad = f(\tilde{\mathbf{r}}_2|E_0, \mathbf{r}_0, \tilde{E}_1, \tilde{\mathbf{r}}_1, t) f(\tilde{E}_1, \tilde{\mathbf{r}}_1, t|E_0, \mathbf{r}_0) \\ &\quad = \frac{1}{4\pi R^2}\, e^{-\mu_{E_0} d_1} N \frac{d\sigma_c(E_0)}{d\Omega}\bigg|_{\tilde{E}_1} \frac{2\pi m_e c^2}{(E_0 - \tilde{E}_1)^2} \\ &\qquad \times \mu_{E_0 - \tilde{E}_1} e^{-\mu_{E_0 - \tilde{E}_1} t} \cdot \frac{\delta(\theta_r - \theta_e)\delta(t - d)}{2\pi t^2 \sin\theta_e}. \end{aligned} \tag{12}$$

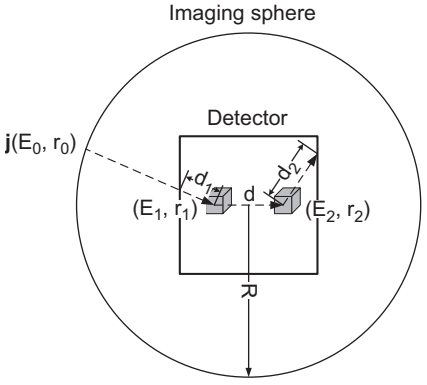

Fig. 3. A photon from pixel **j** creates a two-interaction event **i**, which consists of energy depositions of E_1 and E_2 at positions $\mathbf{r}_1$ and $\mathbf{r}_2$, respectively.

Therefore, given the initial photon has an energy of E_0 and is from $\mathbf{r}_0$, the probability that the first interaction deposits $\tilde{E}_1$ at $\tilde{\mathbf{r}}_1$ and the second interaction happens at $\tilde{\mathbf{r}}_2$ is

$$\begin{aligned} &f(\tilde{E}_1,\tilde{\mathbf{r}}_1,\tilde{\mathbf{r}}_2|E_0,\mathbf{r}_0)\\ &\quad=\int_0^\infty f(\tilde{E}_1,\tilde{\mathbf{r}}_1,t,\tilde{\mathbf{r}}_2|E_0,\mathbf{r}_0)\,\mathrm{d}t\\ &\quad=\frac{1}{4\pi R^2}\,\mathrm{e}^{-\mu_{E_0}d_1}N\frac{\mathrm{d}\sigma_\mathrm{c}(E_0)}{\mathrm{d}\Omega}\bigg|_{\tilde{E}_1}\frac{2\pi m_\mathrm{e}c^2}{(E_0-\tilde{E}_1)^2}\\ &\qquad\times\mu_{E_0-\tilde{E}_1}\mathrm{e}^{-\mu_{E_0-\tilde{E}_1}d}\cdot\frac{\delta(\theta_\mathrm{r}-\theta_\mathrm{e})}{2\pi d^2\sin\theta_\mathrm{e}}. \end{aligned}\tag{13}$$

We will discuss two cases here depending on the type of the second interaction.

(A) *Photopeak events*: The second interaction is a photo absorption, thus the full energy of the incident gamma-ray is deposited in the detector ($(E_0\approx E_1+E_2)$). $f(\tilde{\mathbf{i}}|\mathbf{j})$ becomes

$$\begin{aligned} f(\tilde{\mathbf{i}}|\mathbf{j})&=f(\tilde{E}_1,\tilde{\mathbf{r}}_1,\tilde{E}_2,\tilde{\mathbf{r}}_2|E_0,\mathbf{r}_0)\\ &=f(\tilde{E}_1,\tilde{\mathbf{r}}_1,\tilde{\mathbf{r}}_2|E_0,\mathbf{r}_0)f(\tilde{E}_2|E_0,\mathbf{r}_0,\tilde{E}_1,\tilde{\mathbf{r}}_1,\tilde{\mathbf{r}}_2)\\ &=f(\tilde{E}_1,\tilde{\mathbf{r}}_1,\tilde{\mathbf{r}}_2|E_0,\mathbf{r}_0)\frac{\sigma_\mathrm{p}(\tilde{E}_2)\delta(E_0-\tilde{E}_1-\tilde{E}_2)}{\sigma_\mathrm{t}(\tilde{E}_2)}\\ &=f(\tilde{E}_1,\tilde{\mathbf{r}}_1,\tilde{\mathbf{r}}_2|E_0,\mathbf{r}_0)\frac{N\sigma_\mathrm{p}(\tilde{E}_2)\delta(E_0-\tilde{E}_1-\tilde{E}_2)}{\mu_{E_0-\tilde{E}_1}} \end{aligned}\tag{14}$$

in which $\sigma_\mathrm{p}(\tilde{E}_2)$ is the photoelectric cross-section at energy $\tilde{E}_2$.

(B) *Compton continuum*: The second interaction is a Compton scattering and the scattered photon escapes the detector, thus only partial energy of the incident gamma-ray is deposited in the detector ($(E_0>E_1+E_2)$). $f(\tilde{\mathbf{i}}|\mathbf{j})$ becomes

$$\begin{aligned} f(\tilde{\mathbf{i}}|\mathbf{j})&=f(\tilde{E}_1,\tilde{\mathbf{r}}_1,\tilde{E}_2,\tilde{\mathbf{r}}_2|E_0,\mathbf{r}_0)\\ &=f(\tilde{E}_1,\tilde{\mathbf{r}}_1,\tilde{\mathbf{r}}_2|E_0,\mathbf{r}_0)f(\tilde{E}_2|E_0,\mathbf{r}_0,\tilde{E}_1,\tilde{\mathbf{r}}_1,\tilde{\mathbf{r}}_2)\\ &=f(\tilde{E}_1,\tilde{\mathbf{r}}_1,\tilde{\mathbf{r}}_2|E_0,\mathbf{r}_0)\frac{N}{\mu_{E_0-\tilde{E}_1}}\frac{\mathrm{d}\sigma_\mathrm{c}(E_0-\tilde{E}_1)}{\mathrm{d}\Omega}\bigg|_{\tilde{E}_2}\\ &\quad\times\frac{2\pi m_\mathrm{e}c^2}{(E_0-\tilde{E}_1-\tilde{E}_2)^2}\,\mathrm{e}^{-\mu_{E_0-\tilde{E}_1-\tilde{E}_2}d_2}. \end{aligned}\tag{15}$$

2.2. Uncertainties

Due to detector uncertainties, the observed event is different from the actual event. The probability for a photon emitted from pixel $\mathbf{j}$ to create an observed event $\hat{i}$ can be obtained by the integral of

$$f(\hat{\mathbf{i}}|\mathbf{j})=\int f(\hat{\mathbf{i}}|\tilde{\mathbf{i}})f(\tilde{\mathbf{i}}|\mathbf{j})\,\mathrm{d}\tilde{\mathbf{i}}.\tag{16}$$

Specifically, Eq. (16) can be written as

$$\begin{aligned} &f(\hat{E}_1,\hat{\mathbf{r}}_1,\hat{E}_2,\hat{\mathbf{r}}_2|E_0,\mathbf{r}_0)\\ &\quad=\int f(\hat{E}_1,\hat{\mathbf{r}}_1,\hat{E}_2,\hat{\mathbf{r}}_2|\tilde{E}_1,\tilde{\mathbf{r}}_1,\tilde{E}_2,\tilde{\mathbf{r}}_2)f(\tilde{E}_1,\tilde{\mathbf{r}}_1,\tilde{E}_2,\tilde{\mathbf{r}}_2|E_0,\mathbf{r}_0)\,\mathrm{d}\mathbf{V} \end{aligned}\tag{17}$$

in which, $\mathrm{d}\mathbf{V}$ is the integral volume in the measurement space defined by $\tilde{E}_1,\tilde{\mathbf{r}}_1,\tilde{E}_2$ and $\tilde{\mathbf{r}}_2$.

Suppose the measurements of the energy E and the position (x,y,z) all follow Gaussian distribution with uncertainties of σ_E, σ_x, σ_y, and σ_z, respectively. The probability density function of observing $\hat{E}$ given the actual energy deposition of $\tilde{E}$ is

$$f_E(\hat{E}|\tilde{E})=\frac{1}{\sqrt{2\pi\sigma_{\tilde{E}}^2}}\mathrm{e}^{-((\hat{E}-\tilde{E})^2/2\sigma_{\tilde{E}}^2)}.\tag{18}$$

Similarly, we have

$$f_x(\hat{x}|\tilde{x})=\frac{1}{\sqrt{2\pi\sigma_x^2}}\,\mathrm{e}^{-((\hat{x}-\tilde{x})^2/2\sigma_x^2)}\tag{19}$$

$$f_y(\hat{y}|\tilde{y})=\frac{1}{\sqrt{2\pi\sigma_y^2}}\,\mathrm{e}^{-((\hat{y}-\tilde{y})^2/2\sigma_y^2)}\tag{20}$$

$$f_z(\hat{z}|\tilde{z})=\frac{1}{\sqrt{2\pi\sigma_z^2}}\,\mathrm{e}^{-((\hat{z}-\tilde{z})^2/2\sigma_z^2)}.\tag{21}$$

As a result, $f(\hat{\mathbf{i}}|\tilde{\mathbf{i}})=f(\hat{E}_1,\hat{\mathbf{r}}_1,\hat{E}_2,\hat{\mathbf{r}}_2|\tilde{E}_1,\tilde{\mathbf{r}}_1,\tilde{E}_2,\tilde{\mathbf{r}}_2)$ is a joint Gaussian distribution.

If the uncertainties in energy and position are small enough so that $f(\tilde{E}_1,\tilde{\mathbf{r}}_1,\tilde{E}_2,\tilde{\mathbf{r}}_2|E_0,\mathbf{r}_0)$ varies slowly around $(\hat{E}_1,\hat{\mathbf{r}}_1,\hat{E}_2,\hat{\mathbf{r}}_2)$, $f(\tilde{E}_1,\tilde{\mathbf{r}}_1,\tilde{E}_2,\tilde{\mathbf{r}}_2|E_0,\mathbf{r}_0)$ can be regarded as a constant and taken out of the integral in Eq. (17). Since $\int f(\hat{E}_1,\hat{\mathbf{r}}_1,\hat{E}_2,\hat{\mathbf{r}}_2|\tilde{E}_1,\tilde{\mathbf{r}}_1,\tilde{E}_2,\tilde{\mathbf{r}}_2)\,\mathrm{d}\mathbf{V}=1$, we can approximate $f(\hat{E}_1,\hat{\mathbf{r}}_1,\hat{E}_2,\hat{\mathbf{r}}_2|E_0,\mathbf{r}_0)$ by replacing $(\tilde{E}_1,\tilde{\mathbf{r}}_1,\tilde{E}_2,\tilde{\mathbf{r}}_2)$ with $(\hat{E}_1,\hat{\mathbf{r}}_1,\hat{E}_2,\hat{\mathbf{r}}_2)$ in Eqs. (14) and (15).

The above approximation is usually valid when $\tilde{E}_1+\tilde{E}_2<E_0$, which means the second interaction is a Compton scattering. However, if $\tilde{E}_1+\tilde{E}_2=E_0$, which means the second interaction is a photoelectric absorption, $f(\tilde{E}_1,\tilde{\mathbf{r}}_1,\tilde{E}_2,\tilde{\mathbf{r}}_2|E_0,\mathbf{r}_0)$ has a term of a delta function and cannot be regarded as a constant. In this case, the delta function should be integrated over $\tilde{E}_1$ and $\tilde{E}_2$.

(A) *Photopeak events*: $f(\tilde{\mathbf{i}}|\mathbf{j})$ is obtained by

$$\begin{aligned} &f(\hat{E}_1,\hat{\mathbf{r}}_1,\hat{E}_2,\hat{\mathbf{r}}_2|E_0,\mathbf{r}_0)\\ &\quad=f(\hat{E}_1,\hat{\mathbf{r}}_1,\hat{\mathbf{r}}_2|E_0,\mathbf{r}_0)\frac{N\sigma_\mathrm{p}(\hat{E}_2)}{\mu_{E_0-\hat{E}_1}}\\ &\qquad\times\iint\frac{\mathrm{d}\tilde{E}_1\,\mathrm{d}\tilde{E}_2\delta(E_0-\tilde{E}_1-\tilde{E}_2)}{2\pi\sigma_{E_1}\sigma_{E_2}}\\ &\qquad\times\mathrm{e}^{-((\hat{E}_1-\tilde{E}_1)^2/2\sigma_{E_1}^2)-((\hat{E}_2-\tilde{E}_2)^2/2\sigma_{E_2}^2)}\\ &\quad=f(\hat{E}_1,\hat{\mathbf{r}}_1,\hat{\mathbf{r}}_2|E_0,\mathbf{r}_0)\frac{N\sigma_\mathrm{p}(\hat{E}_2)}{\mu_{E_0-\hat{E}_1}}\\ &\qquad\times\int\frac{\mathrm{d}\tilde{E}_1}{2\pi\sigma_{E_1}\sigma_{E_2}}\,\mathrm{e}^{-((\hat{E}_1-\tilde{E}_1)^2/2\sigma_{\tilde{E}_1}^2)-((E_0-\hat{E}_2-\tilde{E}_1)^2/2\sigma_{E_2}^2)}\\ &\quad=\frac{f(\hat{E}_1,\hat{\mathbf{r}}_1,\hat{\mathbf{r}}_2|E_0,\mathbf{r}_0)N\sigma_\mathrm{p}(\hat{E}_2)}{\mu_{E_0-\hat{E}_1}\sqrt{2\pi(\sigma_{\tilde{E}_1}^2+\sigma_{E_2}^2)}}\,\mathrm{e}^{-((E_0-\hat{E}_1-\hat{E}_2)^2/2(\sigma_{E_1}^2+\sigma_{E_2}^2))}. \end{aligned}\tag{22}$$

(B) *Compton continuum*: From Eq. (15), $f(\tilde{\mathbf{i}}|\mathbf{j})$ is obtained by

$$f(\hat{E}_1,\hat{\mathbf{r}}_1,\hat{E}_2,\hat{\mathbf{r}}_2|E_0,\mathbf{r}_0) = f(\hat{E}_1,\hat{\mathbf{r}}_1,\hat{\mathbf{r}}_2|E_0,\mathbf{r}_0)\frac{N}{\mu_{E_0-\hat{E}_1}}\left.\frac{\mathrm{d}\sigma_e(E_0-\hat{E}_1)}{\mathrm{d}\Omega}\right|_{\hat{E}_2} \times \frac{2\pi m_e c^2}{(E_0-\hat{E}_1-\hat{E}_2)^2}\,\mathrm{e}^{-\mu_{E_0-\hat{E}_1-\hat{E}_2}d_2}. \quad (23)$$

In Eqs. (22) and (23), $f(\hat{E}_1,\hat{\mathbf{r}}_1,\hat{\mathbf{r}}_2|E_0,\mathbf{r}_0)$ is the same as Eq. (13), except $\tilde{E}_1$, $\tilde{\mathbf{r}}_1$, and $\tilde{\mathbf{r}}_2$ are replaced by $\hat{E}_1$, $\hat{\mathbf{r}}_1$, and $\hat{\mathbf{r}}_2$.

2.3. Binning

The binning process is to integrate the probability density function over the bin volume, i.e.

$$t_{ij} = \int_{\Delta\mathbf{V}_i} f(\hat{\mathbf{i}}|\mathbf{j})\,\mathrm{d}\hat{\mathbf{i}} = \int_{\Delta\mathbf{V}_i} f(\hat{E}_1,\hat{\mathbf{r}}_1,\hat{E}_2,\hat{\mathbf{r}}_2|E_0,\mathbf{r}_0)\,\mathrm{d}\hat{\mathbf{i}} \quad (24)$$

in which $\mathrm{d}\hat{\mathbf{i}} = \mathrm{d}\hat{E}_1\,\mathrm{d}\hat{\mathbf{r}}_1\,\mathrm{d}\hat{E}_2\,\mathrm{d}\hat{\mathbf{r}}_2$.

If the bin volume is small enough such that all terms except the delta function in $f(\hat{E}_1,\hat{\mathbf{r}}_1,\hat{E}_2,\hat{\mathbf{r}}_2|E_0,\mathbf{r}_0)$ vary slowly within the bin volume, the integral can be approximated by moving those terms out of the integral.

(A) *Photopeak events*: The system response function is

$$t_{ij} = \int_{\Delta V_i} f(\hat{E}_1,\hat{\mathbf{r}}_1,\hat{E}_2,\hat{\mathbf{r}}_2|E_0,\mathbf{r}_0)\,\mathrm{d}\hat{\mathbf{i}} = \frac{1}{4\pi R^2}\,\mathrm{e}^{-\mu_{E_0}d_1}N\left.\frac{\mathrm{d}\sigma_c(E_0)}{\mathrm{d}\Omega}\right|_{E_1}\frac{2\pi m_e c^2}{(E_0-E_1)^2} \times \mathrm{e}^{-\mu_{E_0-E_1}d}\frac{1}{2\pi d^2\sin\theta_e}\frac{N\sigma_p(E_2)}{\sqrt{2\pi(\sigma_{E_1}^2+\sigma_{E_2}^2)}} \times \mathrm{e}^{-((E_0-E_1-E_2)^2/2(\sigma_{E_1}^2+\sigma_{E_2}^2))}\cdot\int_{\Delta\mathbf{V}_i}\delta(\theta_r-\theta_e)\,\mathrm{d}\hat{\mathbf{i}}. \quad (25)$$

(B) *Compton continuum*: The system response function is

$$t_{ij} = \int_{\Delta\mathbf{V}_i} f(\hat{E}_1,\hat{\mathbf{r}}_1,\hat{E}_2,\hat{\mathbf{r}}_2|E_0,\mathbf{r}_0)\,\mathrm{d}\hat{\mathbf{i}} = \frac{1}{4\pi R^2}\,\mathrm{e}^{-\mu_{E_0}d_1}N\left.\frac{\mathrm{d}\sigma_c(E_0)}{\mathrm{d}\Omega}\right|_{E_1}\frac{2\pi m_e c^2}{(E_0-E_1)^2} \times \mathrm{e}^{-\mu_{E_0-E_1}d}\frac{1}{2\pi d^2\sin\theta_e} \times N\left.\frac{\mathrm{d}\sigma_c(E_0-E_1)}{\mathrm{d}\Omega}\right|_{E_2}\frac{2\pi m_e c^2}{(E_0-E_1-E_2)^2} \times \mathrm{e}^{-\mu_{E_0-E_1-E_2}d_2}\int_{\Delta\mathbf{V}_i}\delta(\theta_r-\theta_e)\,\mathrm{d}\hat{\mathbf{i}}. \quad (26)$$

In both cases, there is an integral of $\int_{\Delta\mathbf{V}_i}\delta(\theta_r-\theta_e)\,\mathrm{d}\hat{\mathbf{i}}$ which needs to be solved. Considering that this integral depends on $\mathbf{r}_0$, $\mathbf{r}_1$, $\mathbf{r}_2$, E_0 and E_1, and the integral volume is a rectangular parallelepiped due to pixellation and digitization, it is formidable to obtain an analytical solution for this integral. Here, we make the following assumptions to ease the calculation:

(1) $\mathbf{r}_0$ is on the back-projection cone defined by $\mathbf{r}_1$, $\mathbf{r}_2$, E_0 and E_1. A Gaussian function with its standard deviation equal to the angular uncertainty will be used to approximate the system response for pixels not on the back-projection cone.
(2) The integral volumes around $\mathbf{r}_1$ and $\mathbf{r}_2$ have the same volume, and are approximated by two spheres with equivalent radius of R_0 as illustrated in Fig. 4.
(3) θ_e is constant in the integral region around E_1.

Under the above assumptions, the integral of $\int_{\Delta\mathbf{V}_i}\delta(\theta_r-\theta_e)\,\mathrm{d}\hat{\mathbf{i}}$ can be calculated by

$$\int_{\Delta\mathbf{V}_i}\delta(\theta_r-\theta_e)\,\mathrm{d}\hat{\mathbf{i}} = \Delta E_1\Delta E_2\int_{\Delta\mathbf{V}_1}\mathrm{d}\hat{\mathbf{r}}_1\int_{\Delta\mathbf{V}_2}\mathrm{d}\hat{\mathbf{r}}_2\delta(\theta_r-\theta_e) = \Delta E_1\Delta E_2\int_{\Delta\mathbf{V}_1}\mathrm{d}\hat{\mathbf{r}}_1\int_{-R_0}^{R_0}\mathrm{d}z\int_S \mathrm{d}s\,\delta(\theta_r-\theta_e). \quad (27)$$

The integral region S consists of those points which satisfy $\theta_r=\theta_e$. Strictly speaking, S is not a plane. However, when $\mathrm{d}\gg R_0$, S can be approximated by a plane. Also, when $\mathrm{d}\gg R_0$, $\mathrm{d}z = \mathrm{d}\cdot\mathrm{d}\theta_r$. As a result, we obtain

$$\int_{\Delta\mathbf{V}_i}\delta(\theta_r-\theta_e)\,\mathrm{d}\hat{\mathbf{i}} = \Delta E_1\Delta E_2 d\int_{\Delta\mathbf{V}_1} S\,\mathrm{d}\hat{\mathbf{r}}_1 = \Delta E_1\Delta E_2 d\int_0^{\pi}\pi(R_0\sin\theta)^2\pi(R_0\sin\theta)^2R_0\sin\theta\,\mathrm{d}\theta = \frac{16}{15}\pi^2R_0^5\,\mathrm{d}\Delta E_1\Delta E_2. \quad (28)$$

2.4. Final result

For source pixel $\mathbf{j}$ of which the gamma-ray initial position is on the back-projection cone defined by $\mathbf{r}_1$, $\mathbf{r}_2$,

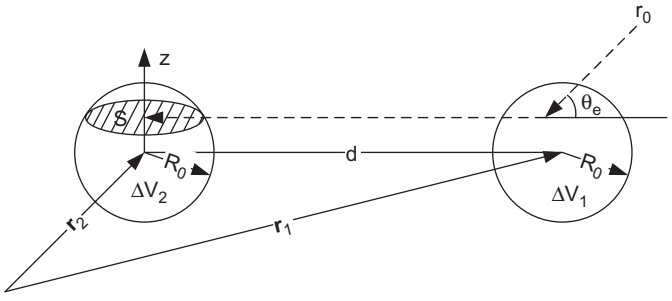

Fig. 4. The bin volumes in the measurement space are approximated by two spheres in calculating the system response function.

E_0 and E_1, the system response function is

(A) *Photopeak events*:

$$t_{ij} = \frac{2R_0^5\Delta E_1\Delta E_2 N^2}{15R^2 d\sin\theta_e}\, e^{-\mu_{E_0} d_1}\frac{d\sigma_c(E_0)}{d\Omega}\bigg|_{E_1}\frac{2\pi m_e c^2}{(E_0-E_1)^2} \times e^{-\mu_{E_0-E_1} d}\frac{\sigma_p(E_2)}{\sqrt{2\pi(\sigma_{E_1}^2+\sigma_{E_2}^2)}} e^{-((E_0-E_1-E_2)^2/2(\sigma_{E_1}^2+\sigma_{E_2}^2))}. \quad (29)$$

(B) *Compton continuum*:

$$t_{ij} = \frac{2R_0^5\Delta E_1\Delta E_2 N^2}{15R^2 d\sin\theta_e}\, e^{-\mu_{E_0} d_1}\frac{d\sigma_c(E_0)}{d\Omega}\bigg|_{E_1}\frac{2\pi m_e c^2}{(E_0-E_1)^2} \times e^{-\mu_{E_0-E_1} d}\frac{d\sigma_c(E_0-E_1)}{d\Omega}\bigg|_{E_2}\frac{2\pi m_e c^2}{(E_0-E_1-E_2)^2} \times e^{-\mu_{E_0-E_1-E_2} d_2}. \quad (30)$$

For other source pixels not on the back-projection cone, their system responses are approximated by a Gaussian function with its standard deviation equal to the angular uncertainty determined by the detector's geometry and energy uncertainties.

In Eqs. (29) and (30), $e^{-\mu_{E_0} d_1}$ is the probability for the incident photon to reach the first interaction position, $d\sigma_c(E_0)/d\Omega|_{E_1} 2\pi m_e c^2/(E_0-E_1)^2$ represents the probability for the incident photon to deposit E_1 in the scattering, $e^{-\mu_{E_0-E_1} d}$ is the probability for the scattered photon to reach the second interaction position, $\sigma_p(E_2)$ represents the probability for the scattered photon to be photoelectrically absorbed, $d\sigma_c(E_0-E_1)/d\Omega|_{E_2} 2\pi m_e c^2/(E_0-E_1-E_2)^2$ represents the probability for the scattered photon to deposit E_2 in the second scattering, and $e^{-\mu_{E_0-E_1-E_2} d_2}$ is the probability for the escaping photon to leave the detector. The $1/\sin\theta_e$ term represents the probability that $\mathbf{r}_2$ is on the direction of the scattered photon. In the Compton continuum case, the lack of the energy Gaussian spread shown in the photopeak case is due to the facts that the system response function in the Compton continuum case is a slow-changing continuous function of the incident gamma-ray energy E_0, and a Gaussian spread with a small uncertainty will not affect the system response function very much. This is the direct result of the approximation done in Eq. (23).

We notice that R_0, ΔE_1, ΔE_2, N and R are all constants for a specific detector system, and d is a fixed value for a specific event. From Eq. (2), the iteration is not sensitive to the scaling factor in the system response function since t_{ij} appears in both the numerator and the denominator. Therefore, we can ignore those constants to simplify the system response function for the two considered cases as follows:

(A) *Photopeak events*:

$$t_{ij} = \frac{1}{\sin\theta_e}\, e^{-\mu_{E_0} d_1}\frac{d\sigma_c(E_0)}{d\Omega}\bigg|_{E_1}\frac{1}{(E_0-E_1)^2} \times e^{-\mu_{E_0-E_1} d}\frac{\sigma_p(E_2)}{\sqrt{2\pi(\sigma_{E_1}^2+\sigma_{E_2}^2)}} e^{-((E_0-E_1-E_2)^2/2(\sigma_{E_1}^2+\sigma_{E_2}^2))}. \quad (31)$$

(B) *Compton continuum*:

$$t_{ij} = \frac{1}{\sin\theta_e}\, e^{-\mu_{E_0} d_1}\frac{d\sigma_c(E_0)}{d\Omega}\bigg|_{E_1}\frac{1}{(E_0-E_1)^2} \times e^{-\mu_{E_0-E_1} d}\frac{d\sigma_c(E_0-E_1)}{d\Omega}\bigg|_{E_2}\frac{2\pi m_e c^2}{(E_0-E_1-E_2)^2} \times e^{-\mu_{E_0-E_1-E_2} d_2}. \quad (32)$$

There are several details that need to be addressed:

(A) *Total cross-section*: The total cross-section may not include the coherent scattering (Rayleigh scattering) cross-section because the photon does not lose energy in coherent scattering process. The coherent scattering is usually unimportant in modeling gamma-ray transportations. However, when the gamma ray energy is low (below a few hundred keV), the cross-section and average deflection angle of the coherent scattering become non-trivial, and the coherent scattering should be taken into account in a complete model.

(B) *Sequence ambiguity*: Because of the poor timing resolution of the three-dimensional position-sensitive CdZnTe detector, it is difficult to tell which interaction occurs first. Various sequencing algorithms have been developed to reconstruct the interaction sequences based on the position and energy information of the interactions [8,10,11]. However, those algorithms can only estimate which sequence has the highest probability. They cannot eliminate the sequence ambiguity. An accurate system response model should consider all the possible sequences. Particularly, for a two-interaction event, each interaction can be the first interaction. Therefore, there are two back-projection rings at each energy in our model of the system response function.

(C) *Conventional Compton cameras*: For conventional Compton cameras with known incident gamma ray energy E_0 and known interaction sequence, the system response function can be greatly simplified due to the insensitivity of the MLEM algorithm to the scaling factors in the system response function. In this case, Eqs. (31) and (32) can both be reduced to $e^{-\sigma_t(E_0) d_1}$, which is the only term in the system response function related to pixel **j**. If the size of the detector system is small, this term can be further reduced. Therefore, the system response function for conventional Compton cameras is constant on the back-projection cone with a spread defined by the angular uncertainties.

(D) *Variation in the binning volume size*: The anode surface of the three-dimensional position-sensitive CdZnTe detector is pixellized into an 11×11 array. The effective volume of the peripheral pixels is slightly larger than that of the center pixels. This variation in the binning volume size will affect the integral of $\int_{\Delta V_i}\delta(\theta_r-\theta_e)\,d\hat{i}$ in the derivation of the system response function. However, this

integral does not depend on the energy or direction of the incident gamma-ray, thus is a constant to all pixels. Again, due to the insensitivity of the MLEM algorithm to the scaling factors in t_{ij}, this integral can be ignored. Therefore, the variation in the binning volume size will not affect the deconvolution process.

3. Performance

The energy-imaging integrated deconvolution algorithm was applied to both simulated and measured data. In the system response function model of Eq. (31), the energy resolution is modeled by

$$\Delta_{\text{overall}}(E) = \sqrt{\Delta_{\text{noise}}^2 + 2.35^2 FEW} \tag{33}$$

in which Δ_{overall} and Δ_{noise} are the full width at half maximum (FWHM) of the overall and electronic noise, E is the gamma-ray energy, the electronic noise Δ_{noise} is set at 5 keV, the Fano factor F is assumed to be 1, and the average ionization energy W is 5 eV for CdZnTe. The spatial imaging space of the 4π sphere was divided into 64×64 pixels, and the energy space was divided into 500 bins from 0 to 2 MeV. The MLEM algorithm was stopped at the 24th iteration for all calculations.

3.1. Simulation

Ideally, the energy-imaging integrated deconvolution algorithm estimates the true incident gamma-ray intensity. A Monte Carlo simulation using Geant4 [12] was performed with a gamma-ray source uniformly distributed from 300 keV to 1 MeV. The source is also uniformly distributed on a circle around the detector, and the gamma-ray energy is a linear function of the source direction, as shown in Fig. 5. By deconvolving the simulation data, we can examine both the energy and spatial uniformity of the deconvolution method.

Fig. 6 shows the simulated two-pixel spectrum and the deconvolved spectrum. About 226k two-pixel events were used in the deconvolution. The simulated raw spectrum does not imply that the source is uniform between 300 keV and 1 MeV. This is because the detection efficiencies at different energies are different, and the low-energy part of the spectrum is contaminated by the Compton background from the high-energy gamma-rays. The simulated raw spectrum also shows a Compton background below 300 keV although there is no incident gamma-ray with energy below 300 keV. However, the deconvolved spectrum represents the true energy distribution of the incident gamma-rays, which is uniform from 300 keV to 1 MeV. Fig. 7 shows the deconvolved energy spectra at different gamma-ray incident directions. The deconvolved spectrum in Fig. 6 still shows some Compton background below 300 keV. This background is caused by the low-detection efficiency for gamma-rays with energy lower than 200 keV, and the MLEM algorithm tends to amplify the statistical

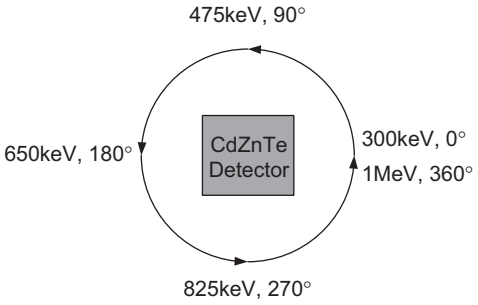

Fig. 5. Source distribution in the Geant4 simulation. The source is uniformly distributed around the sides of the detector. The source energy increases from 300 keV to 1 MeV linearly as a function of the rotational angle from 0° to 360°.

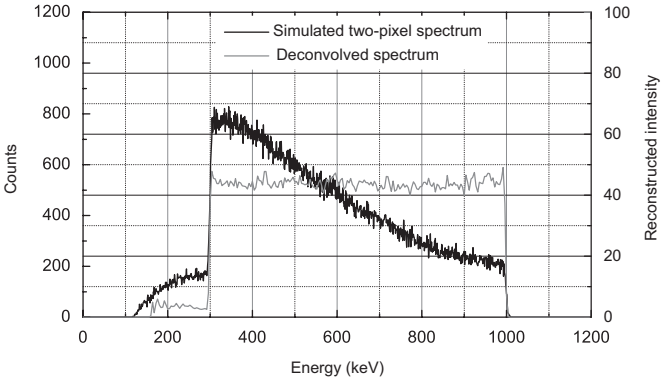

Fig. 6. Simulated two-pixel spectrum and deconvolved spectrum.

noise if the detection efficiency is low. However, in Fig. 7 we can see that the Compton background around 200 keV is distributed across all angles and can be ignored for each direction. Although the detection sensitivity varies according to the incident directions because of the asymmetry of the geometry of the detector, the deconvolved spectra correctly show that the source is spatially uniform.

3.2. Experiment

A single three-dimensional CdZnTe detector was used in the experiment. A ^{137}Cs, a ^{22}Na, and a ^{133}Ba source were placed at three different sides of the three-dimensional CdZnTe detector as shown in Fig. 8. The measured raw two-pixel spectrum is shown in the top figure in Fig. 10, in which a Compton continuum is clearly present. About 41k two-pixel events were measured. After the energy-imaging integrated deconvolution, the three sources were well resolved. Fig. 9 shows the images at the three characteristic energies of the gamma-ray sources, which are 356, 511 and 662 keV. It clearly shows the locations of the three sources. If we look at the directions of the three sources, as shown in Fig. 10, the deconvolved spectra only show the true incident gamma-ray spectra which are free of Compton continuum.

Although the spectral-deconvolution method can remove the Compton continuum which is caused by the

scatters within the detector, it is not able to remove the background in which the scatters occur outside the detector, since those scattered gamma-rays are "true" incident gamma-rays and cannot be distinguished from the unscattered photons. For those events, the gamma-ray from the source is first scattered by the materials surrounding the detector, then the scattered photon enters the detector and is recorded. Since the deconvolved spectra represent the intensity of the incident gamma-rays, which include the scattered photons from the surrounding materials, we expect to see a distribution of those scattered photons, especially a backscatter peak. Fig. 10 also shows the deconvolved spectrum from all directions, which still presents a continuous background. However, because the scattered photons are spatially distributed, their distribution is not prominent in the localized spectrum shown in Fig. 10.

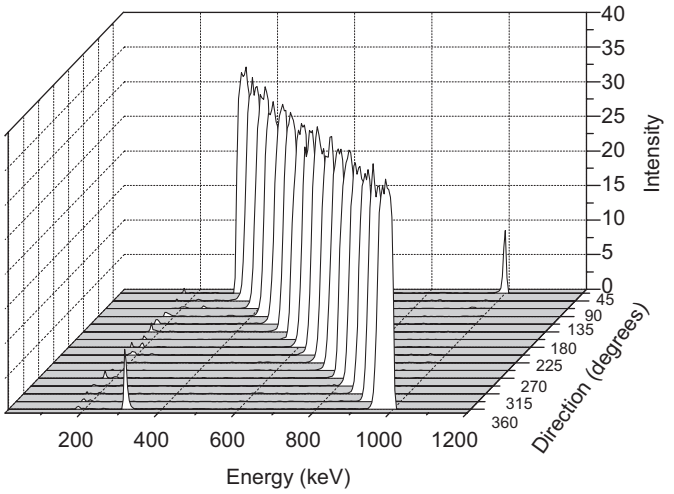

Fig. 7. Deconvolved spectra at different directions. The spectra show that the source is not only uniformly distributed in energy from 300 keV to 1 MeV, but it is also uniformly distributed across spatial directions.

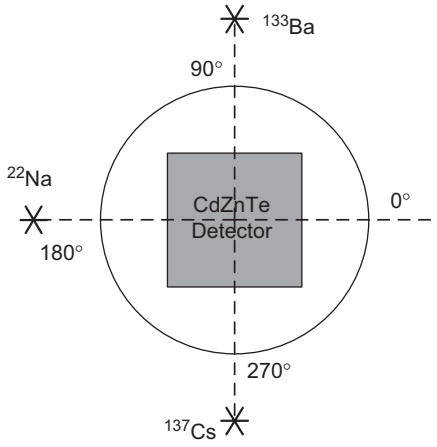

Fig. 8. Experiment setup. Three point sources (a ^{137}Cs, a ^{22}Na and a ^{133}Ba) were placed at three different sides of the three-dimensional CdZnTe detector.

In order to verify that the deconvolved spectrum represents the true intensity of the incident gamma-rays, the relative strength of the four ^{133}Ba gamma lines to the 356 keV line is listed in Table 1. The relative intensities are calculated with background subtracted. As we can see, the deconvolved spectrum represents the true relative intensities much better than the measured raw spectrum.

3.3. Comparison with conventional Compton imaging and spectral deconvolution

Conventional Compton imaging was performed by setting an energy window around the full energy peak. By doing so, the true full energy deposition events as well as the Compton backgrounds from higher energy gamma-rays are selected. The Compton backgrounds are usually spatially distributed. As a result, the Compton backgrounds have little effect on the angular resolution of the reconstructed image of a point source. However, as shown in Fig. 11(a), the Compton backgrounds do introduce noises in the reconstructed image because they are from random directions. Fig. 11(b) shows the energy-imaging integrated deconvolved image summed in the same energy window. The Compton backgrounds are correctly placed in the energy bin of the original gamma-rays. As a result, the Compton backgrounds introduce less noises comparing with the conventional Compton imaging.

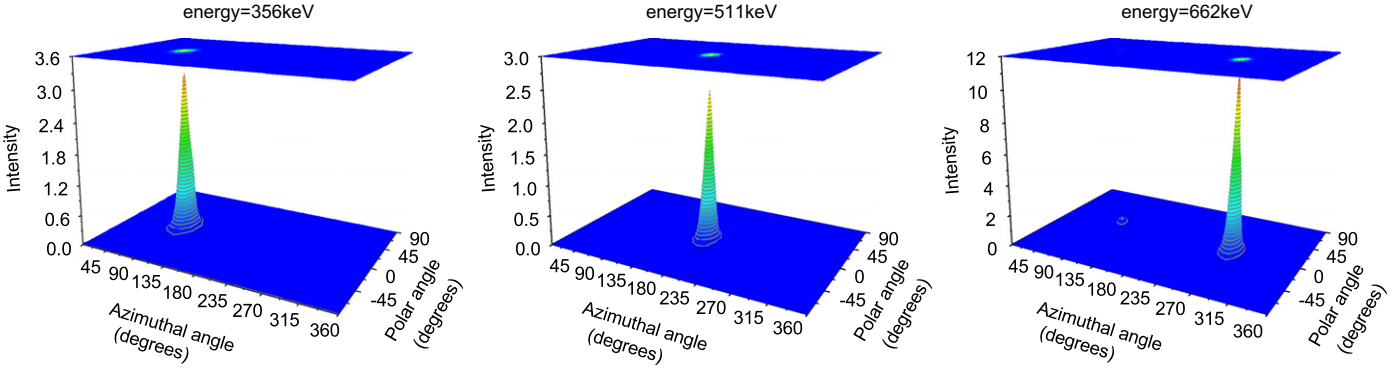

Fig. 9. The deconvolved images at the photopeak energies of the three sources. The 4π imaging space is projected onto a plane defined by the azimuthal and the polar angles of the sphere.

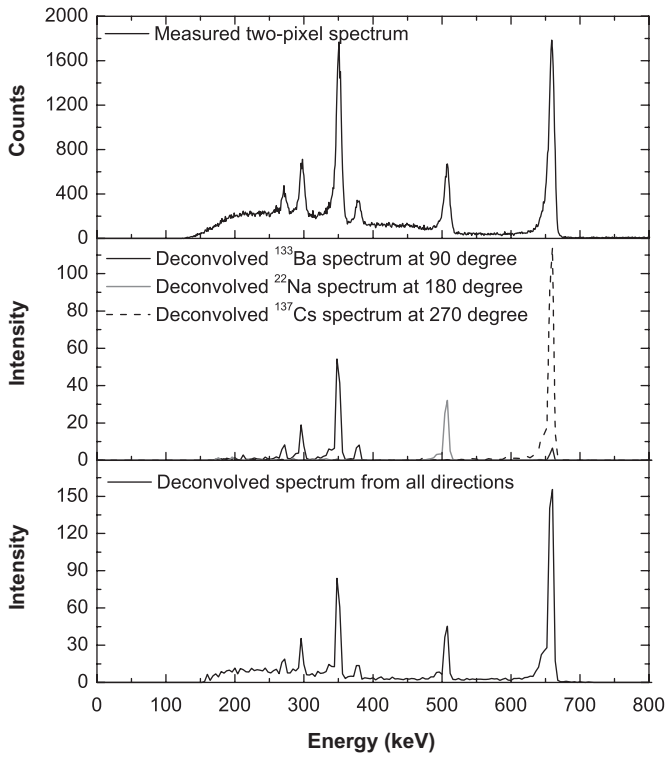

Fig. 10. The upper figure is the measured two-pixel spectrum. The middle figure shows the deconvolved spectra at the three source directions. The lower figure is the deconvolved spectrum from all directions.

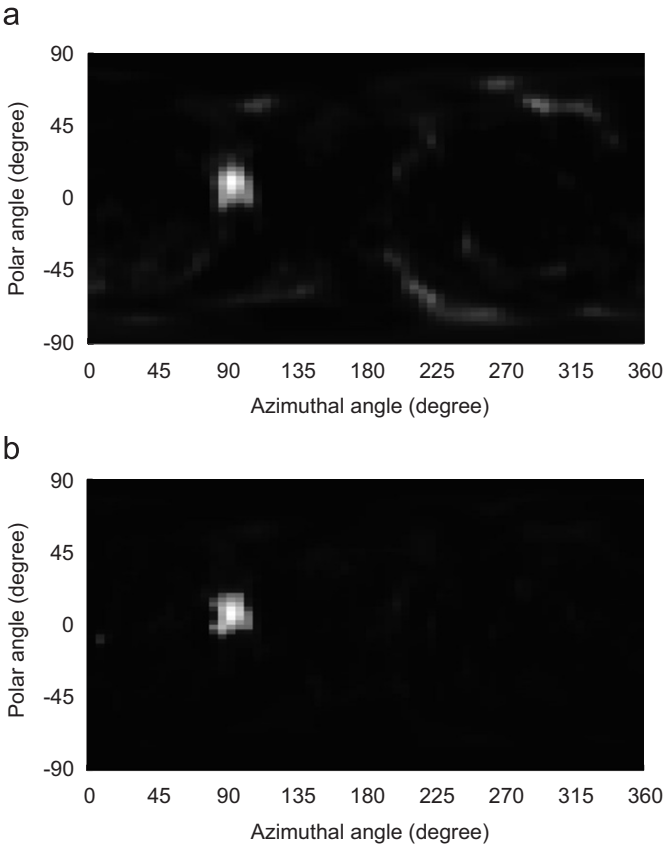

Fig. 11. Images of the 384 keV line from the ^{133}Ba source: (a) Reconstructed image by setting an energy window from 370 to 390 keV. (b) Energy-imaging integrated deconvolved image summed from 370 to 390 keV.

Table 1
Relative intensities of the four ^{133}Ba lines to the 356 keV line

	276 keV	302 keV	356 keV	384 keV
Relative source intensity (%)	11.55	29.54	100	14.41
Measured spectrum (%)	8.87	26.70	100	11.39
Deconvolved spectrum (%)	12.30	29.65	100	14.27

The energy-imaging integrated algorithm uses all measured events and puts the Compton backgrounds into the right energy bin. As a result, the image obtained at a full energy peak is from both the true full energy deposition events and the Compton backgrounds. The Compton backgrounds usually have larger angular uncertainties than the full energy events. Therefore, the imaging spatial resolution of the new imaging-energy integrated deconvolution algorithm is not superior compared to conventional Compton imaging. Fig. 12 shows the images obtained by the two methods for the 511 keV gamma-rays from a ^{22}Na source. It can be seen that the energy-imaging integrated deconvolved image has a spatial resolution slightly worse than the conventionally reconstructed image.

Energy spectral deconvolution was also applied to the measurement. Because it does not require the directional information of the incident gamma-rays, single-pixel events can also be used in the deconvolution. The system response function for the spectral-only deconvolution was obtained by Geant4 simulations. Fig. 13 shows the measured raw spectrum of all events and the deconvolved spectrum. In the spectrum, it can be seen that the 80 keV photopeak from the ^{133}Ba source is also present. In the current system, the energy threshold for individual pixels is about 60 keV. Therefore, for two-pixel events, the minimal detectable energy is 120 keV, which is the reason why the 80 keV peak is absent in the spectra in Fig. 10. Comparing the energy-imaging integrated deconvolved spectrum in Fig. 10 with the spectral deconvolved spectrum in Fig. 13, we can see both spectra show backgrounds due to photons that were scattered outside the detector. Because both methods did not model the surrounding materials, the scattering background cannot be removed by either method. By carefully modeling the surrounding materials, the energy spectral deconvolution method can provide a more detailed system response function and can remove the scattering background. However, this practice is not possible for hand-held detectors of which the operation environment changes frequently. In the energy-imaging integrated deconvolved spectrum, because the scattering background is spatially distributed, the scattering background is not present in the

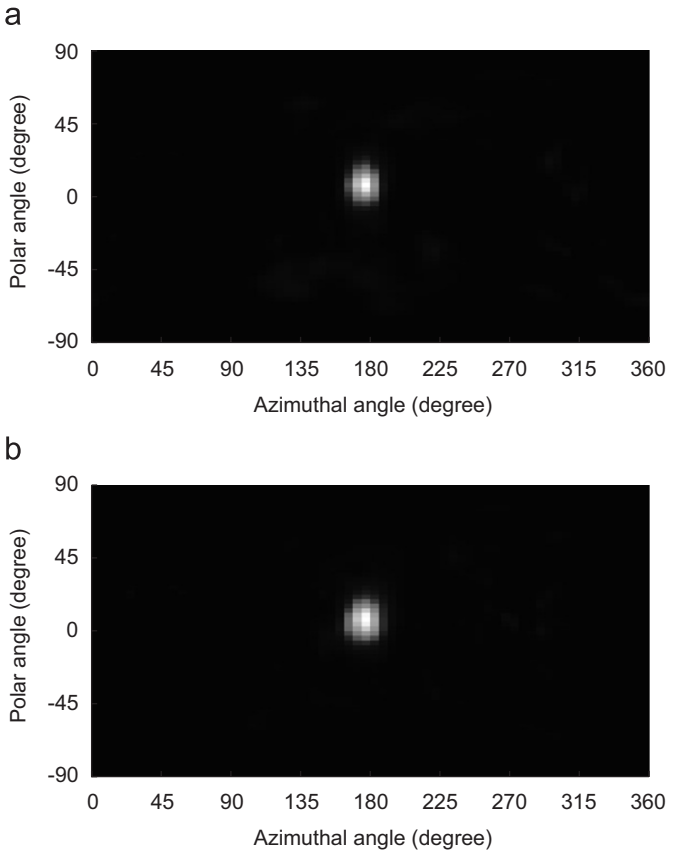

Fig. 12. Images of the 511 keV line from the ^{22}Na source: (a) Reconstructed image by setting an energy window from 490 to 520 keV. (b) Energy-imaging integrated deconvolved image summed from 490 to 520 keV.

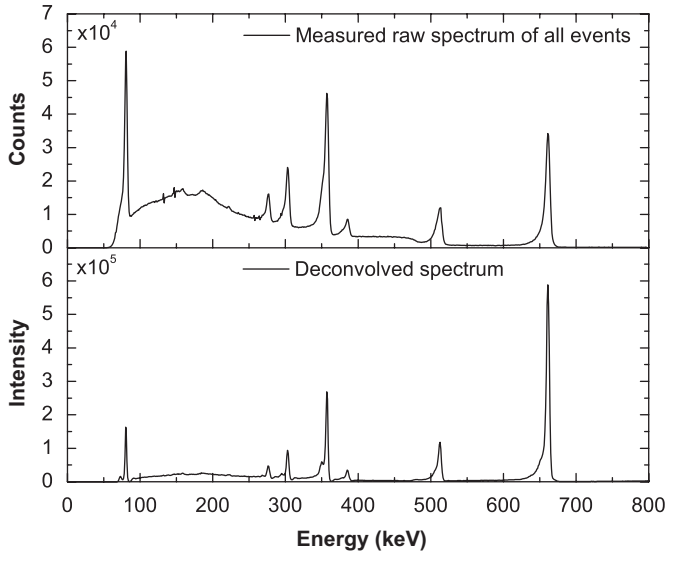

Fig. 13. Energy spectral deconvolution on the measured spectrum. The top figure shows the measured raw spectrum of all events. The bottom figure shows the deconvolved spectrum.

localized spectra at the true source directions. As a result, the signal-to-noise ratio can be improved at the true source directions.

4. Conclusions

Traditional spectral-deconvolution methods are performed only on energy spectra. Since the gamma-ray response of any non-spherical detector depends on the incident direction of the gamma-rays, those algorithms cannot truthfully deconvolve the spectra of spatially distributed sources. Even if the detector is spherical, different surrounding materials will affect the back-scattering and will result in different spectrum responses to the same gamma-ray source. In this work, an imaging procedure is introduced into the spectral-deconvolution process by means of Compton imaging. Modern position-sensitive gamma-ray detector systems can give position information about the gamma-ray interactions in the detector. If more than one interaction is observed in a single event, extra information about the incident gamma-ray's direction can be derived. Therefore, the detector response function can be established as a function of the incident gamma-ray's direction. The proposed energy-imaging integrated deconvolution algorithm takes the advantage of this directional dependence in the system response function, and performs the deconvolution process in a combined spatial and energy space, thus overcoming the difficulties in traditional spectral-deconvolution methods. The deconvolved spectrum is a function of the incident gamma-ray's direction; therefore, it can provide the energy spectrum at any specific direction, as well as the image at any specific energy. This energy-imaging integrated deconvolution algorithm does not need to know the energy of the incident gamma-rays, which is required information in most Compton camera systems.

The MLEM algorithm, which is popular in solving photon-emission image reconstruction problems, is applied in the deconvolution process. Due to the large number of bins of the measurement output, the deconvolution is performed in list-mode. The number of elements in the system response function is so large that it is impossible to pre-calculate the system response function by simulations. An analytical approach is derived to allow the calculation of the system response function during the reconstruction process.

The three-dimensional position-sensitive CdZnTe detector is an instrument which can provide both the position and the energy information of individual gamma-ray interactions. Although the size of the detector is relatively small ($15 \times 15 \times 10\,\text{mm}^3$), the detection efficiency as a Compton imager is much higher than a conventional two-detector Compton imaging system because there is no separation between the first and the second detector. The proposed energy-imaging integrated deconvolution algorithm is applied to the three-dimensional position-sensitive CdZnTe detector with both simulated and measured data. The results show that the new algorithm is capable of deconvolving the energy spectrum and reconstructing the image simultaneously. The deconvolved spectra, as expected, are free of Compton continuum and are the estimations of the true intensities of the incident gamma-rays.

The energy-imaging integrated deconvolution algorithm is not limited to three-dimensional position-sensitive CdZnTe detectors. This algorithm can be applied to any gamma-ray detector system with three-dimensional position-sensitive capability, such as three-dimensional position-sensing germanium, stacks of double-sided silicon strip detectors, depth of interaction (DOI) scintillators, and gas or liquid Xenon time projection chambers (TPC).

References

[1] L. Bouchet, Astron. Astrophys. Suppl. Ser. (113) (1995) 167.
[2] L. Meng, D. Ramsden, IEEE Trans. Nucl. Sci. NS-47 (4) (2000) 1329.
[3] A. Dempster, N. Laird, D. Rubin, J. R. Stat. Soc. B 39 (1) (1977) 1.
[4] L. Shepp, Y. Vardi, IEEE Trans. Med. Imag. MI-1 (1982) 113.
[5] L. Parra, H. Barrett, IEEE Trans. Nucl. Sci. NS-17 (2) (1998) 228.
[6] Z. He, W. Li, G.F. Knoll, D.K. Wehe, J. Berry, C.M. Stahle, Nucl. Instr. and Meth. A 422 (1–3) (1999) 173.
[7] F. Zhang, Z. He, D. Xu, G. Knoll, D. Wehe, J. Berry, IEEE Trans. Nucl. Sci. NS-51 (5) (2004) 2427.
[8] C. Lehner, Z. He, F. Zhang, IEEE Trans. Nucl. Sci. NS-51 (4) (2004) 1618.
[9] D. Xu, Z. He, C.E. Lehner, F. Zhang, Proc. SPIE 5540 (2004) 144.
[10] R. Kroeger, W. Johnson, J. Kurfess, B. Phlips, E. Wulf, IEEE Trans. Nucl. Sci. NS-49 (4) (2002) 1887.
[11] I. Lee, Nucl. Instr. and Meth. A 422 (1999) 195.
[12] S. Agostinelli, J. Allison, K. Amako, J. Apostolakis, H. Araujo, P. Arce, M. Asai, D. Axen, S. Banerjee, G. Barrand, Nucl. Instr. and Meth. A 506 (3) (2003) 250.